ACS APPLIED MATERIALS & INTERFACES

Research Article

www.acsami.org

Kelvin Probe Force Microscopic Imaging of the Energy Barrier and Energetically Favorable Offset of Interfaces in Double-Junction Organic Solar Cells

Mahbube K. Siddiki, Swaminathan Venkatesan, David Galipeau, and Qiquan Qiao*

Center for Advanced Photovoltaics, Department of Electrical Engineering and Computer Sciences, South Dakota State University, Brookings, South Dakota 57006, United States

ABSTRACT: A double-junction polymer solar cell (PSC) has attracted extensive attention as a promising approach to increasing efficiency. Tunneling/recombination interlayers between subcells play a critical role in double-junction PSCs. Interlayers include electron-transport layers (ETLs) such as Nb_2O_5, ZnO, and TiO_x and hole-transport layers (HTLs) including PEDOT:PSS. These materials have all been used as interlayer materials, but it remains unclear which one is better than the other. Kelvin probe force microscopy (KFM) was used to identify the energy barrier and energetically favorable energy offset at the interfaces of acceptor−ETL (e.g., PCBM−Nb_2O_5, PCBM−ZnO, and PCBM−TiO_x) and donor−HTL (e.g., MDMO-PPV/PEDOT:PSS). Here the interface refers to the junction of two materials, formed by drop-casting one on top of other. The interface is buried and is therefore not accessible to the KFM probe. The energy barrier for electron transport from PCBM to ETL was found at ∼0.20, ∼0.12, and ∼0.012 eV at the PCBM−Nb_2O_5, PCBM−ZnO, and PCBM−TiO_x interfaces, respectively. Hole transport from the donor polymer to PEDOT:PSS was found to be energetically favorable with an energy offset of ∼0.14 eV to facilitate hole transport. The thickness independences of the energy barrier and energetically favorable energy offset at the interfaces of acceptor−ETL and donor−HTL were also observed. This work will provide guidance for researchers to identify and select appropriate materials as interlayers in double-junction PSCs.

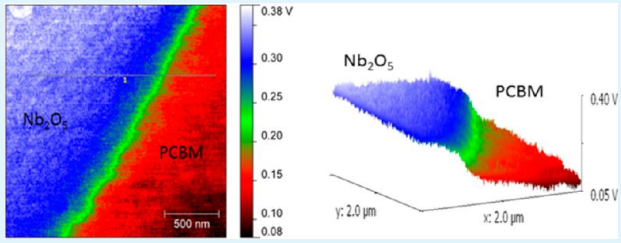

KEYWORDS: *organic photovoltaics, electron-transport layer, hole-transport layer, double junction, multijunction, recombination/tunneling layer*

1. INTRODUCTION

Organic photovoltaics (OPVs) have potential as a low-cost renewable energy source.[1−9] Solution-processable polymer-based OPVs are of particular interest because they can be manufactured by high-throughput roll-to-roll processes.[10,11] Significant progresses have been made in terms of improving the performance of single- and double-junction polymer solar cells (PSCs) with efficiencies (PCEs) of ∼8% and ∼10.6%, respectively. However, the current performance and lifetime of these PSCs are still relatively low compared to their inorganic counterparts. Hence, further improvements are necessary before mass production and practical applications of PSCs take place.

Cell parameters that need to improve urgently in single-junction PSCs include the short-circuit current density (J_{SC}), open-circuit voltage (V_{OC}), and fill factor (FF). However, there are some inherent losses that are difficult to avoid in a single-junction device, which include (i) absorption loss (cannot absorb photons with energy lower than donor bandgaps), (ii) thermalization loss (conversion of the photon energy into excitons with lower energy), (iii) exciton loss−exciton recombination, (iv) energy loss required for exciton dissociation, and (v) charge transport loss (charge trapping and recombination). These limitations and losses reduce the device efficiency far below its predicted value.[6,7] Among all approaches that are used to improve the device efficiencies, one of the most common and successful strategies is to use a multijunction structure. Multijunction devices can reduce these losses significantly by employing two or more separate subcells, with complementary absorption spectra, which convert different regions of the solar spectrum into electricity by different subcells. Individual subcells are connected to each other by interlayers. Commonly used interlayer materials include metal oxides,[12−14] cross-linkable charge-transporting materials,[15−17] conjugated semiconductor electrolytes,[18−20] self-assembled functional molecules,[21,22] and graphene.[23] They are used because of their charge selectivity, optical transparency, and compatibility with all-solution processing.

Transition-metal oxides [e.g., TiO_x ($x \leq 2$), ZnO, Nb_2O_5], transparent conductive oxides such as indium−tin oxide (ITO), metallic nanoclusters (e.g., Au and Ag nanoclusters), and PEDOT derivatives have been used as tunneling/recombination interlayers in polymer multijunction solar cells.[13,14,24,25] The mechanical properties of these layers are important

Received: October 21, 2012
Accepted: January 4, 2013
Published: January 4, 2013

because they act as protecting layers for the bottom subcells and bases for the top subcells. The optical transparency of interlayers needs to be considered along with their electrical properties because light blocking from the interlayers can reduce light that reaches to the back subcells. Metal oxides such as Nb_2O_5, TiO_x ($x \leq 2$), and ZnO are transparent to the visible range and intrinsically n-type and therefore can serve as electron-transport layers (ETLs) for the optical front subcells and as stable bases for the back subcells.[13] Conducting polymers (e.g., PEDOT:PSS and modified PEDOT) and other transitional-metal oxides (e.g., V_2O_5, MoO_3, etc.) can act as hole-transport layers (HTLs).[24] Two or more subcells can be stacked together with the assistance of semitransparent ETLs and HTLs. In addition to their role as ETLs, transitional-metal oxides like TiO_x ($x \leq 2$) and ZnO can also be used as optical spacers. An embedded optical spacer can separate two photoactive single cells and optimize the electronic and optical properties of the entire cells, which benefits PSCs whose film thicknesses are limited by low charge carrier mobility.[14,26]

Double-junction devices with series-connected subcells require careful design and selection of interlayer materials.[7] A few most prominent interfaces include acceptor−ETL and donor−HTL.[27] The contact potential difference (CPD) at these interfaces is preferred to have an energetically favorable offset rather than a barrier to facilitate charge transport.[13] Kelvin probe force microscopy (KFM), developed by Nonnenmacher et al.,[28] is a technique that can determine the local CPD with high spatial resolution. Because the morphology and surface potential of the interfacial and active layers are of utmost important in the energy conversion process in this type of solar cell, a deeper understanding of the tools and techniques like electrical scanning probe microscopy is needed for extracting valuable information of the surface properties of these materials with better accuracy.[29] One needs to be very careful also concerning the contact area between the probe tip and the sample surface as well. A recent study showed that a solar cell performance can be affected by nanoscale as well as micrometer-scale nonuniformities in composition and the electrical properties of the materials used.[30]

Although various ETL layers including Nb_2O_5, ZnO, and TiO_x combined with HTL layers such as PEDOT:PSS have been used as interlayers in double-junction PSCs, little work has been conducted in studying the acceptor−ETL and donor−HTL interfaces. In this work, KFM was used to identify the energy barrier and energy offset at the interfaces of acceptor−ETL (e.g., PCBM-Nb_2O_5, PCBM-ZnO, and PCBM-TiO_x) and donor−HTL (e.g., MDMO-PPV/PEDOT:PSS) that are commonly used as recombination/tunneling interlayers in double-junction cells. The energy barrier for electron transport from PCBM to ETL was identified as ∼0.2, ∼0.12, and ∼0.012 eV at the interfaces of PCBM−Nb_2O_5, PCBM−ZnO, and PCBM−TiO_x, respectively. However, hole transport from the donor polymer (e.g., MDMO-PPV) to PEDOT:PSS was found to be energetically favorable with an energy offset of ∼0.14 eV.

2. EXPERIMENTAL SECTION

Preparation of a Nb_2O_5 Sol−Gel Solution and Nanoparticles. A Nb_2O_5 sol−gel solution was prepared following a previous report.[31] A total of 4.5 mL of niobium ethoxide [$Nb(OC_2H_5)_5$; Aldrich, 99.95%] was mixed with 3 mL of ethanol (99.5%) and 0.015 mL of acetic acid. The mixture was then stirred for 1 h and kept for 1 day. The final solution concentration is 2.21 M. Later the solution was diluted to the desired concentration using ethanol.

Preparation of a ZnO Sol−Gel Solution and Nanoparticles. ZnO nanoparticles were prepared using an adapted procedure reported previously.[32,33] First 125 mL of methanol was heated at 60 °C, followed by the addition of 13.4 mmol of zinc acetate dihydrate (Acros, >98%) under vigorous stirring. The solute dissolved quickly and became clear. A total of 23 mmol of KOH (Fisher Chemical, >85%) was dissolved in 65 mL of methanol to make a clear basic solution, which was then added dropwise to the zinc acetate dihydrate solution. This took ∼10 min. Initially, $Zn(OH)_2$ precipitation was observed, but after a few minutes, it dissolved. After 7−10 min, the solution became translucent and remained so for some time. After ∼1.5 h, the nanoparticles started to precipitate and the solution became turbid. Then after ∼2.5 h from the time of nanoparticle formation, the heater and stirrer were shut down and the nanoparticles were allowed to precipitate for an additional 2.5 h, which amassed at the bottom of the flask. The precipitate was separated from the mother liquor by decantation and then washed twice by adding 50 mL of methanol each time. The suspension was left unstirred for at least 1 h to reach full precipitation. After decantation of the solvent from the top, the suspension was centrifuged to get rid of the remaining solvent. Later acetone was added to the centrifuged nanoparticles and then sonicated for ∼1 h to make a uniform suspension.

Preparation of a TiO_x Sol−Gel Solution and Nanoparticles. A TiO_x sol−gel solution was prepared following previous reports in an inert atmosphere.[13,34] Titanium(IV) isopropoxide ($Ti[OCH(CH_3)_2]_4$, Acros Organic, 99%, 10 mL) as a precursor was mixed with 2-methoxyethanol ($CH_3OCH_2CH_2OH$, Aldrich, 99.9+%, 50 mL) and ethanolamine ($H_2NCH_2CH_2OH$, Aldrich, 99+%, 5 mL) in a three-necked flask. The three necks were connected with a condenser, thermometer, and nitrogen gas inlet/outlet, respectively. Then, the mixed solution was heated to 80 °C for 2 h in a silicon oil bath with magnetic stirring and then 120 °C for 1 h more. This two-step heating (80 and 120 °C) was repeated one more time, and then the solution was allowed to cool slowly. The as-prepared typical TiO_x sol−gel solution was diluted in isopropyl alcohol to the desired concentration.

Preparation of a PCBM and MDMO-PPV Solution. [6,6]-Phenyl-C61-butyric acid methyl ester (PCBM, 99.5% purity, Nano-C) was dissolved in chlorobenzene at a concentration of 12 mg/mL. Poly[2-methoxy-5-(3′,7′-dimethyloctyloxy)-1,4-phenylenevinylene] (MDMO-PPV, American Dye Source Inc.) was dissolved in chlorobenzene. Neutral-pH PEDOT (Orgacon, batch 5541073, pH 7, 1.2 wt %) was collected from Agfa Gevaert NV.

Preparation of PCBM−Nb_2O_5, PCBM−ZnO, and PCBM−TiO_x Interfaces. ITO glass substrates (Delta Technologies, 8−12 Ω/square) were cleaned with soapy water, deionized water, acetone, and isopropyl alcohol (99.5%) for 10 min each with sonication. The substrates were dried under a N_2 flux and finally treated for 20 min in an oxygen plasma cleaner (Harrick Plasma).

A PCBM solution was spin-coated on cleaned ITO glass at a spin speed of 1500 rpm for 60 s. The film was dried at room temperature for 5 min with a thickness of ∼100 nm. A Nb_2O_5 sol−gel solution was then drop-casted on a PCBM film using a micropipet. Drop-casting was done carefully to avoid scratching the PCBM film because the pipet tip was taken very close to the surface of the PCBM film. The layer of Nb_2O_5 sol−gel solution was allowed to spread slowly while being dried to form an interface. No further heating was used. Three to four different drop-casted interfaces were made on the same substrate to enhance the probability to obtain at least one interface, which is clearly visible and free of void and cracks under an optical microscope. The selected best interface was used for KFM imaging. PCBM−ZnO and PCBM−TiO_x interfaces were also made by drop-casting similar to that for the PCBM−Nb_2O_5 interface. PCBM−ZnO was prepared at room temperature without further heating; however, the PCBM−TiO_x interface was heated at 80 °C in air for 10 min in order for oxide formation after drop-casting, as suggested by Kim et al.[13]

Preparation of a PEDOT:PSS/MDMO-PPV Interface. This interface was made in a fashion similar to that described in a previous section. PEDOT:PSS was spin-coated on clean ITO glass substrates at a spin speed of 5000 rpm for 60 s. The substrate was dried up at room

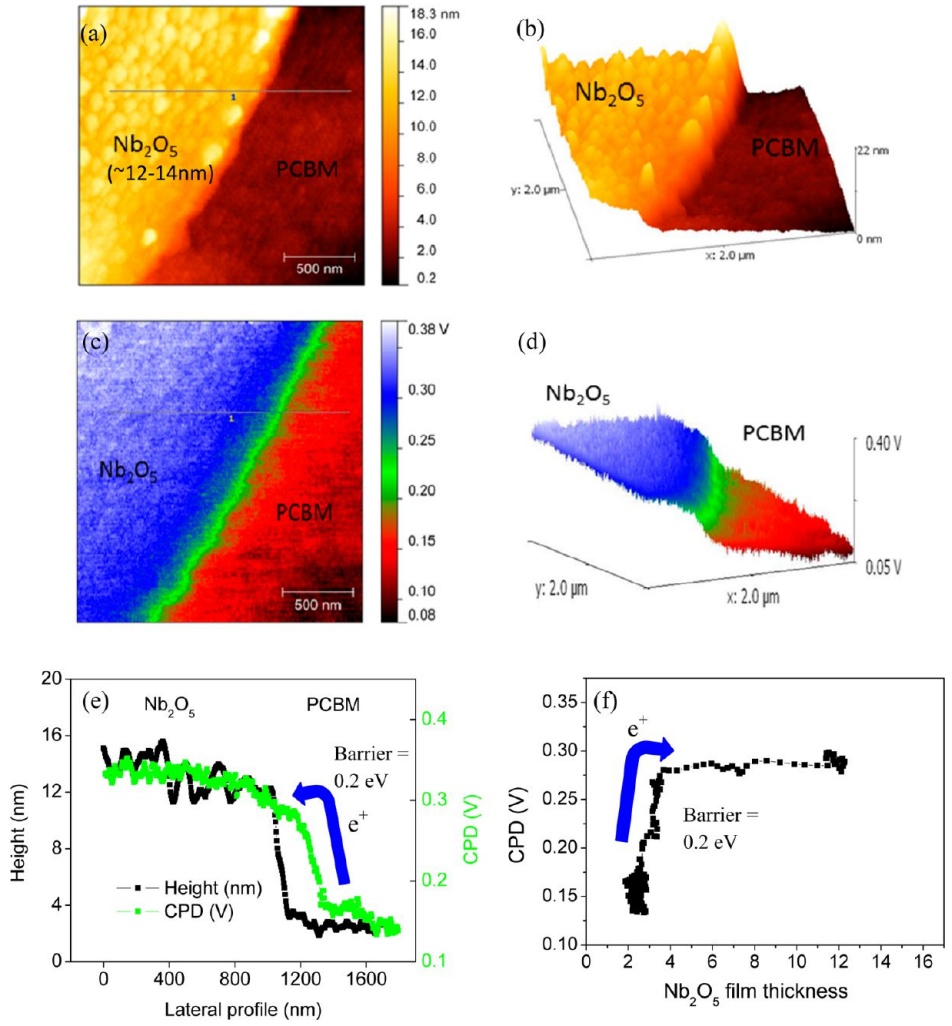

Figure 1. Surface topography images of PCBM−Nb_2O_5 layers and their interface in (a) 2D and (b) 3D views. CPD images of PCBM−Nb_2O_5 layers and their interface in (c) 2D and (d) 3D views. (e) Height and CPD versus the lateral profile across the PCBM−Nb_2O_5 interface. (f) CPD versus the Nb_2O_5 film thickness, which was ∼12−14 nm.

temperature. A MDMO-PPV solution was drop-casted on top of PEDOT:PSS. No further heating of the substrate was done.

KFM Imaging. In KFM, the CPD between the tip and sample is measured along with topography. In this method, the tip is given an electrical oscillation, which induces an electrostatic force between the tip and sample. This electrostatic force is nullified by applying the direct-current (dc) bias offset on the scanning tip at every pixel on the sample. This potential is actually the CPD between the tip and sample, namely, the work function difference between them. AFM images were taken using an Agilent SPM 5500 atomic force microscope equipped with a MAC III controller (comprising three lock-in amplifiers), in tapping mode. A Budget Sensors' Multi 75-EG probe having a platinum/iridium conductive coating was used as the tip. The tip's first resonance (f_1) of 63 kHz was fed into the first lock-in amplifier (LIA1). LIA1 provides the error in the amplitude signal at f_1 to the servo that controls the vertical tip−sample separation. This servo loop is used for topographic imaging, while the second resonant frequency (f_2) of the tip, which was 405 kHz, was fed into the second lock-in amplifier (LIA2) for KFM. LIA2 provides an electrical oscillation to the tip at f_2 with a certain dc offset to induce an electrostatic force between the tip and sample. The phase of the second lock-in amplifier is adjusted to maximize the X component of the amplitude and minimize the Y component of the LIA2. This electrostatic amplitude in our case was attained with a dc offset of −1.2 V for all samples, and the drive percentage of LIA2 was adjusted to attain approximately an amplitude of 0.2 V for LIA2. In KFM, an external dc servo is used that nullifies the electrostatic interaction by applying a certain dc bias to the tip. This dc bias recorded at each point gives the local CPD or surface potential and hence the images of KFM are constructed using the pixel coordinates. Prior to KFM measurements, CPD versus Z spectroscopy were done at both interfaces and small changes were made to the dc servo set point to maintain a constant CPD. This is the set point that the internal dc servo tries to maintain and is basically an internal hardware calibration.[35] Also, for the purpose of reducing errors in the CPD values due to surface absorbates, e.g., moisture or solvent itself, the samples were dried under high vacuum and later were kept in a N_2-filled glovebox. Measurement was carried out immediately after the samples were taken out of the glovebox, and during imaging, the sample holder was always covered to avoid any external light.[36]

3. RESULT AND ANALYSIS

AFM and KFM Micrographs of a PCBM−Nb_2O_5 Interface. Parts a and b of Figure 1 show AFM surface topography images of PCBM−Nb_2O_5 layers and their interface in 2D and 3D views. The brighter granular part on the left side of the images was from Nb_2O_5, while the darker right side was from PCBM. Nb_2O_5 nanoparticles were much larger compared to PCBM. The interface of the two layers was formed when Nb_2O_5 was deposited on the top of PCBM, which left a clearly visible step in the 3D image. Nb_2O_5 nanoparticles formed a compact layer, and the height of the step between Nb_2O_5 and

dx.doi.org/10.1021/am302235w | ACS Appl. Mater. Interfaces 2013, 5, 1279−1286

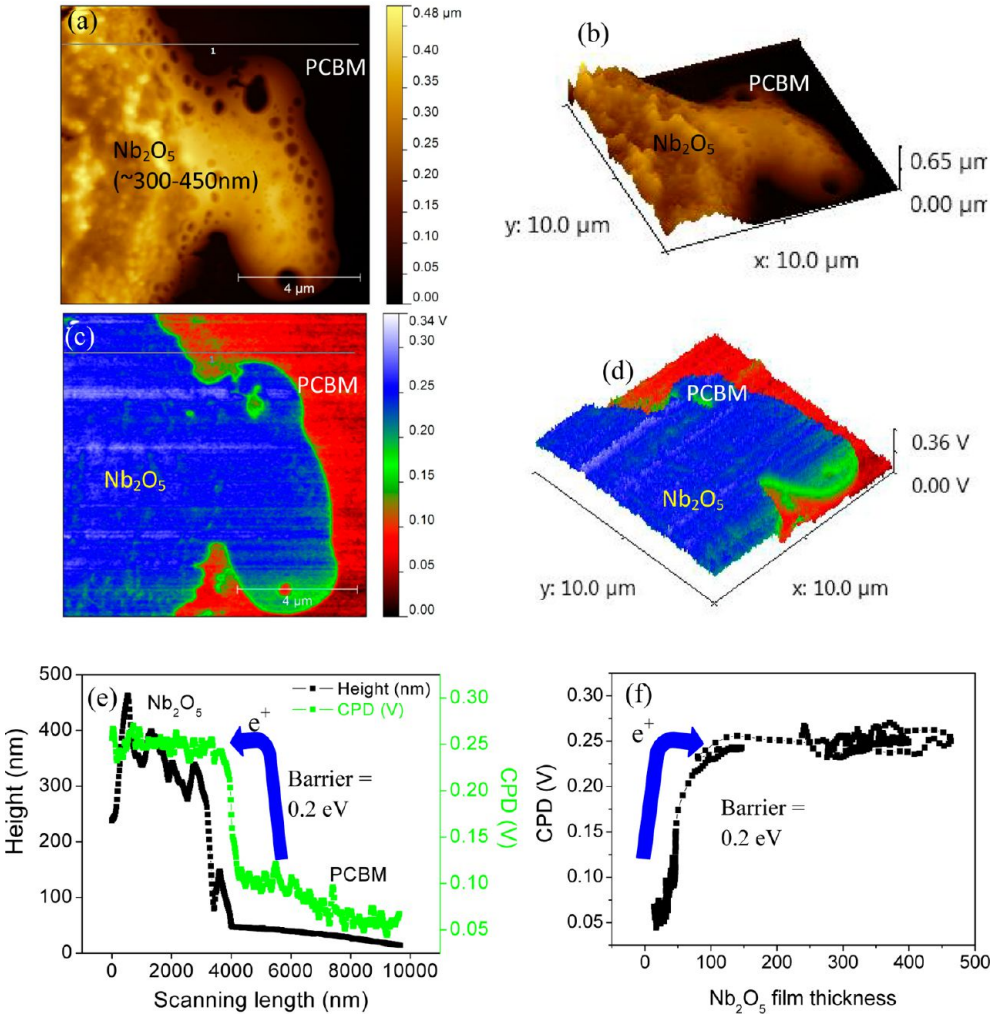

Figure 2. Surface topography images of PCBM−Nb_2O_5 layers and their interface in 2D (a) and 3D (b) views. CPD images of PCBM−Nb_2O_5 layers and the interface in 2D (c) and 3D (d) views. (e) Height and CPD versus the lateral profile across the PCBM−Nb_2O_5 interface. (f) CPD versus the Nb_2O_5 film thickness.

PCBM (i.e., Nb_2O_5 film thickness) was ~12−14 nm. The image indicates no cluster formation on the PCBM side, which appears to be smoother. A robust interfacial layer can be formed with these two materials from their precursor solutions.

Parts c and d of Figure 1 show KFM CPD images of the Nb_2O_5−PCBM layers and their interface in 2D and 3D views. The differences of the CPD between these two layers and their interface are represented as color variations. The blue part is due to Nb_2O_5, whereas the red part is due to PCBM. Both materials are electron transporters in nature. Nb_2O_5 has a higher CPD than PCBM. The green line dividing these two distinct parts might be due to intermixing of these two materials by diffusion. The CPD difference between those two layers was found to be approximately 0.2 V, which can act as a barrier for electron transport from PCBM to Nb_2O_5. Such a barrier can the reduce double-junction PSC performance.

Figure 1e shows the height and CPD versus the lateral profile at the PCBM−Nb_2O_5 interface based on Figure 1a,c. The black line shows the lateral height profile, whereas the green line shows the CPD of the scanned line (labeled 1) in Figure 1a,c. On the Nb_2O_5 side, there was a significant height variation, but the average CPD did not change significantly, indicating that roughness/heights had little effect on the CPD. A CPD difference of ~0.2 V was observed at the PCBM−Nb_2O_5 interface, which will act as a barrier for electrons to transport from PCBM to Nb_2O_5. This might contribute to the series resistance in the optical front cell, thus reducing FF.

Figure 1f shows the CPD versus the Nb_2O_5 thickness. It can be seen that, as the Nb_2O_5 thickness increases from 4 to 12 nm, the CPD remains almost constant. However, the CPD at the PCBM−Nb_2O_5 interface shows some change in thickness from 2 to 4 nm, which might be caused by the intermixing of these two materials due to diffusion.

In order to study the effects of large thicknesses on CPD, a thick film (400 nm) of Nb_2O_5 was also deposited on PCBM. Figure 2 shows the surface topography and KFM CPD images in 2D (a and c) and 3D (b and d) views. In the surface topography images (Figure 2a,b), the yellow part represents Nb_2O_5, whereas the black part represents PCBM. Similarly, in the CPD images (Figure 2c,d), the left-side blue region is from Nb_2O_5, whereas the right-side red region is from PCBM. Figure 2e shows the height and CPD versus the lateral profile across the PCBM−Nb_2O_5 interface. The Nb_2O_5 film thickness was ~300−450 nm, and a CPD difference of ~0.2 V was found at the interface of Nb_2O_5 and PCBM, which could act as a barrier for electrons to transport from PCBM to Nb_2O_5 and contribute to the series resistance in the cells, thus reducing the cell performance. Figure 2f shows CPD versus the Nb_2O_5 thickness.

dx.doi.org/10.1021/am302235w | ACS Appl. Mater. Interfaces 2013, 5, 1279−1286

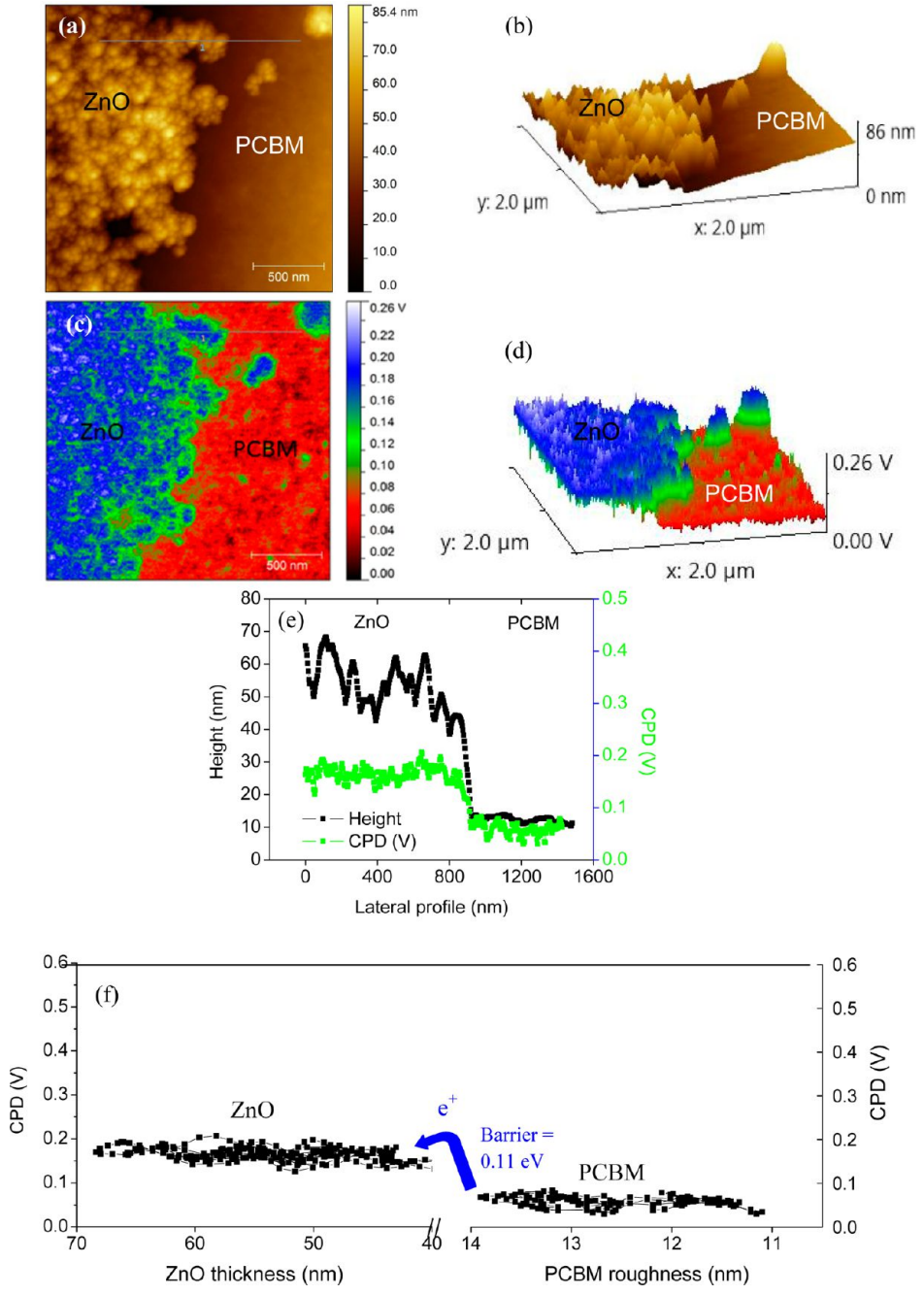

Figure 3. AFM surface topography images of PCBM−ZnO layers and their interface in (a) 2D and (b) 3D views. KFM CPD images of PCBM−ZnO layers and their interface in (c) 2D and (d) 3D views. (e) Height and CPD diagram versus the lateral profile across the PCBM−ZnO interface. (f) CPD versus the ZnO thickness.

The CPD remains almost constant as the Nb_2O_5 thickness increases from 100 to 450 nm. The CPD at a thickness below 100 nm was from PCBM.

AFM and KFM Micrographs of the PCBM−ZnO Interface. Parts a and b of Figure 3 show AFM surface topography images of PCBM−ZnO layers and their interface in 2D and 3D views. The brighter granular region on the left was due to ZnO nanoparticles, while the darker smooth part on the right was due to PCBM. This indicated that ∼10−15 nm ZnO nanoparticles were larger than those of PCBM. The interface was formed by depositing ZnO on the top of PCBM, which formed a step of ∼80−90 nm height. No clusters were found on the PCBM side. There was no dissolution or defect during the deposition of ZnO onto PCBM, indicating the possibility that a robust interfacial layer can be formed with these two materials from their corresponding precursor solutions.

Parts c and d of Figure 3 show KFM CPD images of the PCBM−ZnO films and their interface in 2D and 3D views, respectively. The blue region on the left side was from ZnO nanoparticles, while the red region was from PCBM, indicating that ZnO had a higher CPD than that of PCBM. The green line separating the two sides was attributed to the intermixing of ZnO and PCBM due to diffusion. The CPD difference between ZnO and PCBM layers was ∼0.12 V, which might act as a barrier for electron transport from PCBM to ZnO.

dx.doi.org/10.1021/am302235w | ACS Appl. Mater. Interfaces 2013, 5, 1279−1286

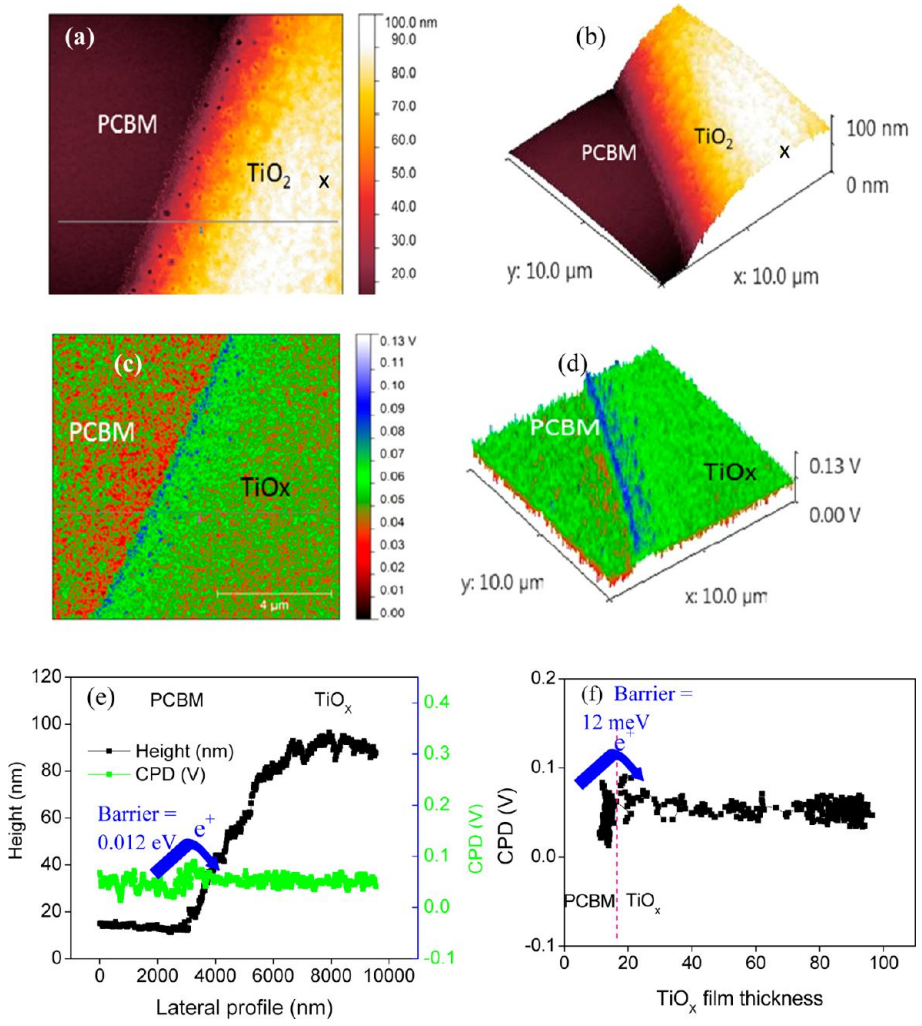

Figure 4. AFM surface topography image of PCBM−TiO_x layers and their interface in (a) 2D and (b) 3D views. KFM CPD images of the PCBM−TiO_x layers and their interface in (c) 2D and (d) 3D views. (e) Height and CPD diagram versus the lateral profile across the interface of PCBM−TiO_x. (f) CPD versus the TiO_x film thickness.

Figure 3e shows height and CPD versus the lateral profile across the PCBM−ZnO interface. The black and green lines are the height and CPD, respectively. The ZnO side has several peaks and valleys, but the CPD does not change significantly, indicating that roughness/thickness variation had little effect on the surface potential. The left part of Figure 3f shows a thickness-independent CPD on the ZnO layer. A 0.11 V CPD between ZnO and PCBM was found at their interface. Compared to Nb_2O_5, the barrier energy for electron transport is less. However, it still may affect electron transport from PCBM to ZnO.

AFM and KFM Micrographs of the PCBM−TiO_x Interface. Parts a and b of Figure 4 show AFM surface topography images of the PCBM−TiO_x film and their interface in (a) 2D and (b) 3D views. The darker part on the left side and the brighter granular part on the right side were due to PCBM and TiO_x, respectively. The TiO_x nanoparticle size ranged between 10 and 15 nm and was larger than that of PCBM. The interface of the PCBM−TiO_x layers formed when TiO_x was deposited on the top of PCBM, which left a visible step in the 3D image (Figure 4b), with a height of around 85−90 nm. The result indicated that the PCBM layer did not form clusters and there was no dissolution or defect at the interface, indicating the possibility of a robust interfacial layer formation with these two materials and their corresponding precursor solutions.

Parts c and d of Figure 4 show KFM CPD images of the PCBM−TiO_x layers and their interface in 2D and 3D views. The left part, which is rich in red with green dots, was from PCBM, and the right side of the image, which is green, was from TiO_x. The blue line dividing the two sides was the intermixing of these two materials due to diffusion. TiO_x had a slightly higher CPD than that of PCBM. The result also indicated that the CPD difference between these two layers was ~0.012 V, far less than that of the PCBM−Nb_2O_5 and PCBM−ZnO interfaces.

Figure 4e shows the height and CPD versus the lateral profile across the PCBM−TiO_x interface. The black line was the height, while the green line was the CPD. The result indicated that, unlike Nb_2O_5 and ZnO, the energy barrier for electron transport from PCBM to TiO_x can be neglected because of the low CPD difference (~0.012 V) between PCBM and TiO_x. Several peaks and valleys and a slope were on the TiO_x side in the surface topography images, but their corresponding CPD remained almost unchanged, as shown on the TiO_x side in Figure 4f, indicating that roughness/thickness variation had almost no effect on the CPD.

dx.doi.org/10.1021/am302235w | ACS Appl. Mater. Interfaces 2013, 5, 1279−1286

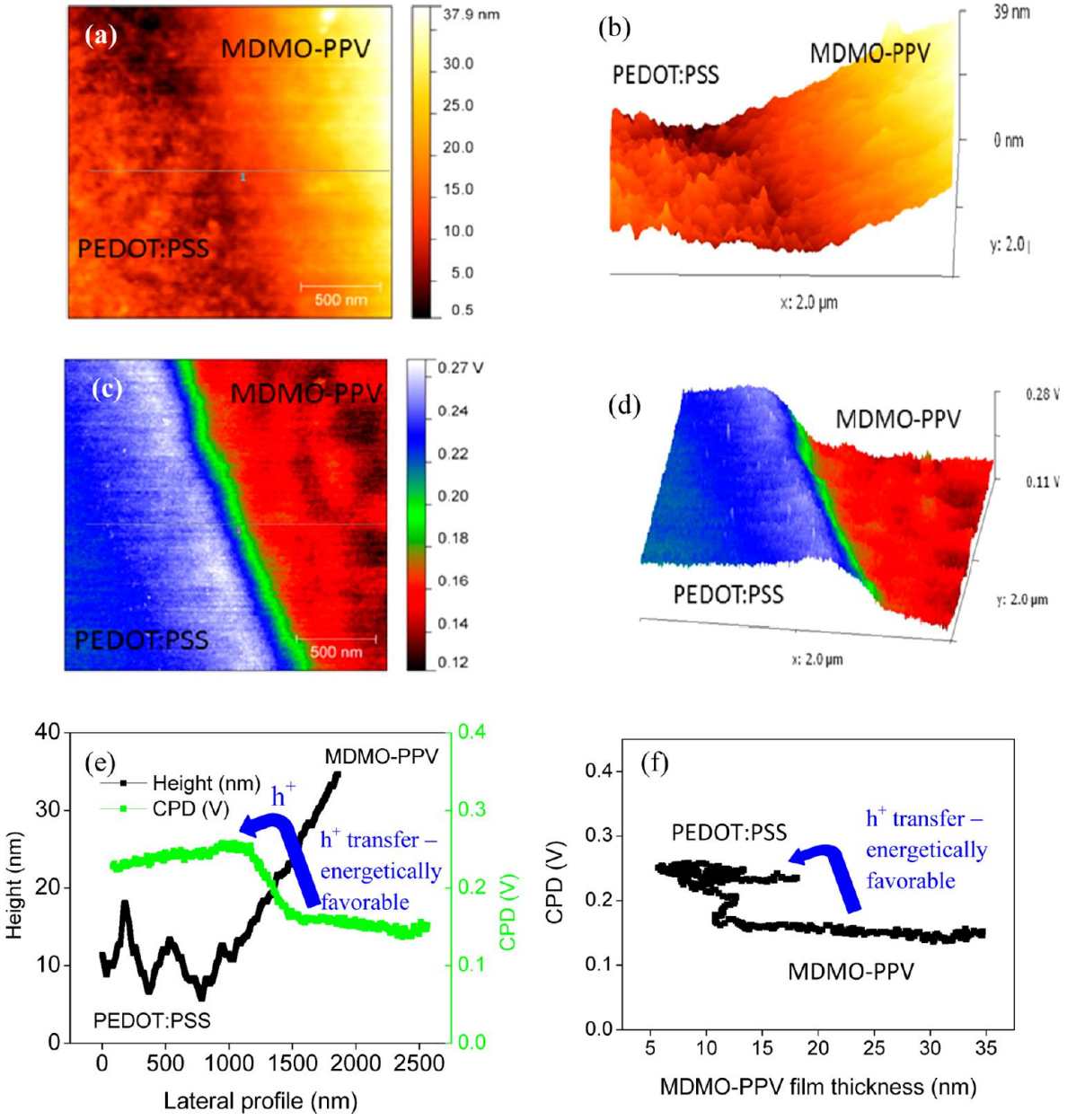

Figure 5. AFM surface topography images of the PEDOT:PSS and MDMO-PPV layers and their interface in (a) 2D and (b) 3D views. KFM CPD images of the MDMO-PPV and PEDOT:PSS layers and their interface in (c) 2D and (d) 3D views. (e) Surface topography and CPD diagram versus the lateral profile across the MDMO-PPV/PEDOT:PSS interface. (f) CPD versus the MDMO-PPV film thickness.

AFM and KFM Micrographs of the PEDOT:PSS/MDMO-PPV Interface. Parts a and b of Figure 5 show AFM surface topography images of the PEDOT:PSS and MDMO-PPV layers and their interfaces in 2D and 3D views. The rough surface on the left side of the image was PEDOT:PSS, while the smooth surface with a slope on the right side was MDMO-PPV. The roughness of PEDOT:PSS was attributed to incomplete dissolution in water. Parts a and b of Figure 5 show that there is a clear boundary between PEDOT:PSS and MDMO-PPV at the interface.

Parts c and d of Figure 5 show KFM CPD images of the PEDOT:PSS (left blue) and MDMO-PPV (right red) layers and their interface in (a) 2D and (b) 3D views. The green line at the interface was attributed to the intermixing of PEDOT:PSS and MDMO-PPV due to diffusion. The 3D image indicates that the CPD difference at the interface was approximately 0.14 V, which was energetically favorable for hole transport from MDMO-PPV to PEDOT:PSS.

Figure 5e shows the height and CPD versus the lateral profile across the MDMO-PPV/PEDOT:PSS interface. The CPD and topographic diagrams were taken from parts a and c of Figure 5, respectively. The height profile showing the slope after the interface with a height of ~28 nm indicates that the PEDOT:PSS side had several peaks and valleys and the thickness increased on the MDMO-PPV side, but the corresponding CPD did not change significantly, indicating that the surface roughness/thickness had little effect on the CPD. The CPD profile versus the thickness in Figure 5f further showed that the CPD difference at the interface was approximately 0.14 V, which was energetically favorable for hole transport from MDMO-PPV to PEDOT:PSS. In addition,

dx.doi.org/10.1021/am302235w | ACS Appl. Mater. Interfaces 2013, 5, 1279–1286

Figure 5f also shows that the CPD is almost independent of the thicknesses of PEDOT:PSS and MDMO-PPV.

CONCLUSION

The development of interlayers with the desired charge selectivity, transport, and compatibility for double-junction PSCs is important to further improve the OPV performance. Deposition of tunneling/recombination interlayers between subcells is one critical step in fabricating highly efficient double-junction PSCs. KFM was used to study the interfaces of PCBM−Nb_2O_5, PCBM−ZnO, and PCBM−TiO_x and polymer−PEDOT:PSS intercell layers in double-junction PSCs. The energy barriers for electron transport are ∼0.20, ∼0.12, and ∼0.012 eV at the interfaces of PCBM−Nb_2O_5, PCBM−ZnO, and PCBM−TiO_x, respectively (Table 1). Hole transport from the donor polymer (e.g., MDMO-PPV) to PEDOT:PSS is energetically favorable with an energy offset of ∼0.14 eV to facilitate hole transport. The thickness independences of the energy barrier and energetically favorable energy offset at the interfaces of acceptor−ETL and donor−HTL were also observed.

Table 1. Energy Barrier (eV) and Energetically Favorable Offset (eV) for Charge Transport in the Interlayers between Subcells

material	energy barrier (eV)	energetically favorable energy offset (eV)
Nb_2O_5−PCBM	0.2	
ZnO−PCBM	0.11	
TiO_x−PCBM	0.012	
PEDOT:PSS/MDMO-PPV		0.14

AUTHOR INFORMATION

Corresponding Author

*E-mail: Qiquan.qiao@sdstate.edu.

Notes

The authors declare no competing financial interest.

ACKNOWLEDGMENTS

This work benefited from the U.S.−Egypt Joint Program, NSF CAREER Program (ECCS-0950731), NSF/EPSCoR program (Grant 0903804), and SD BoR Competitive Research Grant Program (CRGP).

REFERENCES

(1) Chen, W.; Xu, T.; He, F.; Wang, W.; Wang, C.; Strzalka, J.; Liu, Y.; Wen, J.; Miller, D. J.; Chen, J.; Hong, K.; Yu, L.; Darling, S. B. *Nano Lett.* **2011**, *11*, 3707−3713.
(2) Darling, S. B. *Energy Environ. Sci.* **2009**, *2*, 1266−1273.
(3) Zhang, W.; Xu, Y.; Wang, H.; Xu, C.; Yang, S. *Sol. Energy Mater. Sol. Cells* **2011**, *95*, 2880−2885.
(4) Bi, D.; Wu, F.; Qu, Q.; Yue, W.; Cui, Q.; Shen, W.; Chen, R.; Liu, C.; Qiu, Z.; Wang, M. *J. Phys. Chem. C* **2011**, *115*, 3745−3752.
(5) Xia, Y.; Sun, K.; Ouyang, J. *Energy Environ. Sci.* **2012**, *5*, 5325−5332.
(6) Qiao, Q.; McLeskey, J. T. *Appl. Phys. Lett.* **2005**, *86*, 153501.
(7) Siddiki, M. K.; Li, J.; Galipeau, D.; Qiao, Q. *Energy Environ. Sci.* **2010**, *3*, 867−883.
(8) Xie, Y.; Bao, Y.; Du, J.; Jiang, C.; Qiao, Q. *Phys. Chem. Chem. Phys.* **2012**, *14*, 10168−10177.
(9) Siddiki, M. K.; Venkatesan, S.; Wang, M.; Qiao, Q. *Sol. Energy Mater. Sol. Cells* **2013**, *108*, 225−229.
(10) Zhang, H.; Ouyang, J. *Appl. Phys. Lett.* **2010**, *97*, 063509.
(11) Xu, T.; Qiao, Q. *Energy Environ. Sci.* **2011**, *4*, 2700−2720.
(12) Sista, S.; Park, M.-H.; Hong, Z.; Wu, Y.; Hou, J.; Kwan, W. L.; Li, G.; Yang, Y. *Adv. Mater.* **2010**, *22*, 380−383.
(13) Kim, J. Y.; Lee, K.; Coates, N. E.; Moses, D.; Nguyen, T. Q.; Dante, M.; Heeger, A. J. *Science* **2007**, *317*, 222−225.
(14) Gilot, J.; Wienk, M. M.; Janssen, R. A. J. *Appl. Phys. Lett.* **2007**, *90*, 143512.
(15) Huang, F.; Cheng, Y.-J.; Zhang, Y.; Liu, M. S.; Jen, A. K. Y. *J. Mater. Chem.* **2008**, *18*, 4495−4509.
(16) Sun, Y. *Appl. Phys. Lett.* **2010**, *97*, 193310.
(17) Sun, Y.; Chien, S.-C.; Yip, H.-L.; Zhang, Y.; Chen, K.-S.; Zeigler, D. F.; Chen, F.-C.; Lin, B.; Jen, A. K. Y. *Chem. Mater.* **2011**, *23*, 5006−5015.
(18) Oh, S.-H.; Na, S.-I.; Jo, J.; Lim, B.; Vak, D.; Kim, D.-Y. *Adv. Funct. Mater.* **2010**, *20*, 1977−1983.
(19) Zhao, Y.; Xie, Z.; Qin, C.; Qu, Y.; Geng, Y.; Wang, L. *Sol. Energy Mater. Sol. Cells* **2009**, *93*, 604−608.
(20) Yao, K.; Chen, L.; Chen, Y.; Li, F.; Wang, P. *J. Mater. Chem.* **2011**, *21*, 13780−13784.
(21) Yip, H.-L.; Hau, S. K.; Baek, N. S.; Ma, H.; Jen, A. K. Y. *Adv. Mater.* **2008**, *20*, 2376−2382.
(22) Khodabakhsh, S.; Sanderson, B. M.; Nelson, J.; Jones, T. S. *Adv. Funct. Mater.* **2006**, *16*, 95−100.
(23) Gruner, G. *J. Mater. Chem.* **2006**, *16*, 3533−3539.
(24) Zhao, D. W.; Sun, X. W.; Jiang, C. Y.; Kyaw, A. K. K.; Lo, G. Q.; Kwong, D. L. *IEEE Electron Device Lett.* **2009**, *30*, 490−492.
(25) Louwet, F.; Groenendaal, L.; Dhaen, J.; Manca, J.; Van Luppen, J.; Verdonck, E.; Leenders, L. *Synth. Met.* **2003**, *135−136*, 115−117.
(26) Park, S. H.; Roy, A.; Beaupre, S.; Cho, S.; Coates, N.; Moon, J. S.; Moses, D.; Leclerc, M.; Lee, K.; Heeger, A. J. *Nat. Photon.* **2009**, *3*, 297−302.
(27) Siddiki, M. K.; Venkatesan, S.; Qiao, Q. *Phys. Chem. Chem. Phys.* **2012**, *14*, 4682−4686.
(28) Nonnenmacher, M.; Boyle, M. P. O.; Wickramasinghe, H. K. *Appl. Phys. Lett.* **1991**, *58*, 2921−2923.
(29) Chen, W.; Nikiforov, M. P.; Darling, S. B. *Energy Environ. Sci.* **2012**, *5*, 8045−8074.
(30) Nikiforov, M. P.; Darling, S. B. *Prog. Photovolt.: Res. Appl.* **2012**.
(31) Lira-Cantu, M.; Khoda Siddiki, M.; Muñoz-Rojas, D.; Amade, R.; González-Pech, N. I. *Sol. Energy Mater. Sol. Cells* **2010**, *94*, 1227−1234.
(32) Claudia Pacholski, A. K.; Weller, H. *Angew. Chem., Int. Ed.* **2002**, *41*, 1188−1191.
(33) Gilot, J.; Wienk, M. M.; Janssen, R. A. J. *Adv. Mater.* **2010**, *22*, E67−E71.
(34) Kim, J. Y.; S., H. K.; Lee, H.-H.; Lee, K.; Ma, W.; Gong, X.; Heeger, A. J. *Adv. Mater.* **2006**, *18*, 572−576.
(35) Agilent Technologies 5500 Scanning Probe Microscope. http://www.charfac.umn.edu/instruments/5500_Users_Guide.pdf, accessed Dec 7th, 2012.
(36) Kalinin, S. V.; Bonnell, D. A. *Phys. Rev. B* **2001**, *63*, 125411.